PERGAMON

International Journal of Multiphase Flow 28 (2002) 1631–1657

International Journal of Multiphase Flow

www.elsevier.com/locate/ijmulflow

Quasi-steady deformation and drag of uncontaminated liquid drops

B.T. Helenbrook [a,*], C.F. Edwards [b]

[a] *Department of Mechanical and Aeronautical Engineering, Clarkson University, Potsdam, NY 13699-5725, USA*
[b] *Department of Mechanical Engineering, Stanford University, Stanford, CA 94305-3032, USA*

Received 19 October 2001; received in revised form 26 June 2002

Abstract

Over 3000 fully resolved numerical simulations have been performed of axisymmetric liquid drops in a uniform gaseous stream. By applying a body force, the drops were held at a fixed velocity relative to the gas in order to determine their quasi-steady deformation response. The solutions were obtained using a new two-fluid spectral/hp finite element method which, as determined by validation tests, is accurate to within 1% for the conditions studied. Liquid-to-gas density ratios between 5 and 500, viscosity ratios between 5 and 15, Weber numbers between 0.1 and 50, and Ohnesorge numbers between 10^{-4} and 10 were studied, enabling us to better understand the droplet behavior. Three distinct drop shapes (prolate, oblate, and dimpled) were observed, and the conditions that cause the appearance of these shapes were determined. This allowed a correlation to be developed for predicting the drop shape as a function of the dimensionless parameters governing the system. In addition, a simple criterion predicting the onset of a three-dimensional instability associated with a tumbling motion of the drops was determined. In investigating the drag force on the drops, we found that the current correlations for estimating the effect of internal circulation on the drag for spherical drops were inaccurate and therefore proposed a new correlation. Using this and the deformation correlation, we created a drag model for deforming liquid drops. This model predicts the correct trends in all cases and is usually within 5% of the numerical results. Near break-up, the error becomes larger due to the large deformations in drop shape.

Keywords: Drop; Deformation; Drag; Internal circulation

* Corresponding author. Tel.: +315-268-2204.
E-mail address: helenbrk@clarkson.edu (B.T. Helenbrook).
URL: http://www.clarkson.edu/mae/faculty/helenbrook.html.

0301-9322/02/$ - see front matter
PII: S0301-9322(02)00073-3

1. Introduction

Most methods for modeling a liquid spray require information on the behavior of an individual liquid drop in a gaseous flow. This typically includes the drag force on the drop, the drop's evaporation rate, a drop merging model for collisions, and a drop break-up model. Simplified models for predicting these phenomena have been developed through analytic, experimental, and numerical studies of individual liquid drops. Because of the complex behavior of liquid drops however, there are still many effects which are neglected in the models. One such effect is the deformation of the drop; most models assume a spherical shape. In this paper, we report the results of numerical simulations of a non-evaporating, isolated, liquid drop to quantify the deformation response of a drop. We also examine the drag force on the drop and propose an improved model for drag by incorporating the effects of both deformation and internal circulation.

Drop behavior is examined in a uniform approach flow. This is a canonical problem for sprays because in many applications the drops are smaller than the flow scales and the flow appears uniform to the drop. Experimental data for this flow has been obtained predominantly from drop-tower and shock-tube experiments (see Hsiang and Faeth, 1992) and has been used to develop and validate the current drop models. However, it is difficult to systematically explore the entire parameter space relevant to sprays using either type of experiment. By performing numerical simulations, we can extend the experimental work by obtaining precise information on both the drop shape and the drag for a wide range of conditions. This enables us to provide new insights and examine conditions that are difficult to study experimentally.

Another difficulty in studying drops is their extreme sensitivity to surface contaminants (Clift et al., 1978). Most systems are, to some degree, affected by surface contaminants. Because it is often difficult or impossible to determine the degree/nature of the contamination, we examine uncontaminated drops to bound this limit of drop behavior. Haywood et al. (1994) have postulated that the main effect of contaminants is to reduce the magnitude of the circulation velocity in the interior of the drop. If this is the case, the results we obtain with "small" liquid velocities are relevant to contaminated drops. We have performed some preliminary simulations with contaminants to examine these effects. These can be found in Helenbrook and Edwards (2000).

The most relevant previous numerical studies of drops are those by Dandy and Leal (1989) and by Haywood et al. (1994). These studies examined axisymmetric falling drops and categorized the drop shapes, drag response, and flow fields at various conditions. This work extends those efforts including more than 3000 simulations over a range of practically relevant conditions. The ability to perform this study is due to a spectral/hp finite element algorithm we have developed for simulating two-phase flows which is both accurate and efficient for obtaining steady-state drop solutions. This algorithm is described and validated in Helenbrook (2001).

The paper begins with a formulation of the problem and a discussion of the governing non-dimensional parameters, the physically relevant range of these parameters, and the accuracy of the approximations made in the formulation over this range. This is followed by a summary of the numerical method and the validation results presented in Helenbrook (2001). The remaining sections examine the results. First, we present the most frequently observed drop shapes and give a brief explanation of the mechanisms causing these shapes. This is followed by a more detailed discussion of the parameters controlling the transition between the different shapes and the development of an algebraic correlation for predicting the drop shape. The remaining two sections

focus on the drag force. The first analyzes the effect of internal circulation on the drag for spherical drops, and the second examines the effect of drop deformation on the drag. In these sections, an algebraic correlation is developed for predicting the drag on a deformed liquid drop.

2. Formulation

The physical problem is that of an axisymmetric liquid drop driven through a quiescent gas by a body force such as gravity. We study the deformation and drag of the drop at its terminal velocity, U. This problem is relevant not only to systems with gravity, but also to spray systems in which the drop size is small relative to the flow scales and the injected drop's deformation rate is fast relative to its velocity decay rate. The conditions under which the latter of these two requirements is satisfied will be analyzed after we introduce the non-dimensional parameters governing the problem.

Assuming that the drop velocities are small relative to the speed of sound, we approximate both the gas and the liquid as incompressible. We also neglect temperature gradients and evaporation. This is appropriate for saturated isothermal systems and possibly for vaporizing systems when the evaporation velocity is small relative to the gas velocity, and temperature changes across drop length scales are small. Neglecting temperature gradients is consistent with assuming that the drop is small relative to the flow scales, but there can still be strong gradients if the ambient gas temperature is much larger than the boiling point of the drop.

We can model the above conditions as two fluids with constant densities, ρ_L and ρ_G, and viscosities, μ_L and μ_G, separated by an interface with constant surface tension, σ. The subscripts denote either liquid or gas. Both fluids must satisfy the axisymmetric form of the incompressible Navier–Stokes equations. At the interface, we enforce the conditions that the mass flux through the interface is zero and that the jump in stress across the interface is balanced by surface tension. For the mathematical form of the governing equations and the interface conditions, see Helenbrook (2001).

3. Physical parameters

In the above formulation, there are four independent dimensionless parameters. We choose the liquid-to-gas density ratio ρ_L/ρ_G, the liquid-to-gas dynamic viscosity ratio μ_L/μ_G, the Weber number $We = \rho_G U^2 d/\sigma$, and the Ohnesorge number, $Oh = \mu_L/\sqrt{\rho_L \sigma d}$ to describe the problem, (d is the volume-equivalent diameter of the drop). The body force on the drop does not appear in any of the independent parameters because we have assumed the drop is at its terminal velocity. At the terminal velocity, the body force and the drop velocity are not independent.

For a given pair of fluids (such as hexane/air), the liquid-to-gas density ratio varies mainly with the gas density which is a function of the ambient pressure and temperature. For most spray systems, the pressures are between atmospheric and the critical pressure of the liquid, and the temperatures are between atmospheric temperature and 2500 K, a typical adiabatic flame temperature. To investigate the effect of density ratio over this range of conditions, we study density ratios of 5, 50, and 500. The liquid-to-gas viscosity ratio is primarily a function of the temperature. If we

Table 1
Simulation conditions

ρ_L/ρ_G	μ_L/μ_G	Oh_{min}	Oh_{max}
5	5	0.01	6.3
5	10	0.05	12.6
5	15	0.05	20.0
50	5	0.005	3.15
50	10	0.01	6.3
50	15	0.01	6.3
500	5	0.00063	0.4
500	10	0.001	0.63
500	15	0.008	2.0

Oh increases by factors of $10^{0.2}$. At each *Oh*, *We* increases from 0.1 by factors of $10^{0.1}$.

assume that the gas temperature varies between ambient and 2500 K while the liquid temperature is fixed near the boiling temperature, the viscosity ratio varies between 5 and 15. We study the values 5, 10, and 15. It is somewhat inconsistent with our formulation to assume that the gas temperature is much greater than the liquid temperature because we have neglected temperature gradients, but by examining this range, we can bound the effect of viscosity ratio.

Results are obtained by fixing the Ohnesorge number and increasing the Weber number from a small value, usually 0.1 or less, to a value around 10 in factors of $10^{0.1}$–1.26. At Weber numbers greater than 10, we approach the critical Weber number of break-up. In this paper, we are only interested in the deformation and drag response and will not study the break-up limits. For fixed fluid properties, *Oh* only varies with drop diameter, thus increasing the Weber number with *Oh* held constant corresponds to an experiment in which drops of a fixed size are driven through a flow at increasing velocities.

The smallest Ohnesorge number for which we can study deformation is determined by the axisymmetric assumption. From simulations of flow over a solid sphere, we know that at a Reynolds number, $Re = \rho_G U d/\mu_G$, of around 200 the flow becomes non-axisymmetric (Johnson and Patel, 1999). Since high-viscosity-ratio liquid drops behave similarly to solid spheres, we expect a similar transition. Expressing *Oh* as $\sqrt{\rho_G/\rho_L}(\mu_L/\mu_G)\sqrt{We}/Re$, we see that, for a fixed Weber number and given fluid properties, the smallest *Oh* is determined by the maximum Reynolds number. In obtaining the results for given values of ρ_L/ρ_G and μ_L/μ_G, the smallest *Oh* is chosen such that at $We = 1$, $Re \approx 200$. *Oh* is increased from this value by factors of $10^{0.2}$–1.58 over two to three orders of magnitude. At the largest values of *Oh* the Reynolds number is then $O(10^{-1})$. Table 1 summarizes the range of conditions studied.

4. Time scale analysis

To determine the conditions under which the steady response of a drop to an applied body force is representative of injected drops, we analyze the time scales in the problem. If the velocity decay rate of the drop is small relative to its deformation response rate, the velocity decay will not be important in determining the drop shape. Physically, this means that the drop will respond in a

quasi-steady manner to the instantaneous relative velocity between the drop and the gas even though this velocity is changing with time.

The velocity decay rate of the center of mass of the drop can be estimated assuming that the drag on the drop is similar to that on a solid sphere. Using the Stokes drag law, $C_D = 24/Re$, where C_D is the coefficient of drag given by $8D/(\rho_G U^2 \pi d^2)$ with D being the magnitude of the drag force, we arrive at an exponential decay rate for the drop velocity of $18(\rho_G/p_L)v_G/d^2$ where v_G is the kinematic viscosity of the gas.

Estimates the of deformation rates of an isolated liquid drop can be found in Lamb (1945), Subramanyam (1969), Miller and Scriven (1968) among others. When the Ohnesorge number is much less than one, the drops are under damped, and the oscillation decay rate is given by $20v_L/d^2$ (Miller and Scriven, 1968). If we divide this by the velocity decay rate of a drop in a gas we arrive at 10/9 (μ_L/μ_G). Thus, under damped drops will respond in a quasi-steady manner to the flow if the liquid-to-gas viscosity ratio is large. For the conditions we are studying, this is a reasonable leading order approximation.

When the Ohnesorge number is much greater than one, the drops are over damped and the deformation rate can be estimated as $40\sigma/(19d\mu_L)$ (Miller and Scriven, 1968). Dividing by the velocity decay rate, we arrive at the ratio $20/(171Oh^2)\ \mu_L/\mu_G$. Thus, when the Ohnesorge number is of order $\sqrt{\mu_L/\mu_G}$, the quasi-steady approximation breaks down. In this limit, our simulations will only be relevant to falling liquid drops and not to injected drops. Under these conditions, drop-tower and shock-tube experimental results will also be significantly different.

In addition to the relaxation of the drop shape, it is also important that the drop's internal circulation equilibrate rapidly relative to the velocity decay rate of the center of mass. A simple estimate of the characteristic rate associated with diffusion of momentum into the drop is given by v_L/d^2. Comparing this to the exponential decay rate for the drop velocity, we arrive at μ_L/μ_G. Thus, as long as the liquid-to-gas viscosity ratio is large, the flow in the interior of the drop will respond in a quasi-steady manner to the gas flow velocity.

5. Numerical method

The numerical method we use to perform the calculations is an arbitrary-Lagrangian–Eulerian (ALE) mesh movement scheme with an unstructured mesh. The governing equations are discretized using a spectral/hp finite element approach. The combination of ALE and higher-order elements results in higher-order spatial accuracy for interfacial problems. As we will show shortly, this allows very accurate solutions to be obtained. Detailed information about the method is given in Helenbrook (2001).

We note that there have been several minor changes made to the method described in Helenbrook (2001) to allow improved calculations of quasi-steady drops. First, the ALE mesh movement scheme used to deform the mesh with the liquid interface has been modified to produce better quality meshes for two-fluid problems. The new mesh-movement method is described in Helenbrook (in press). Second, the iterative method used to determine the final position of the interface has been modified to be more efficient over a wider range of conditions. This will be described in a forthcoming paper. Last, the iterative solution procedure was modified so that the

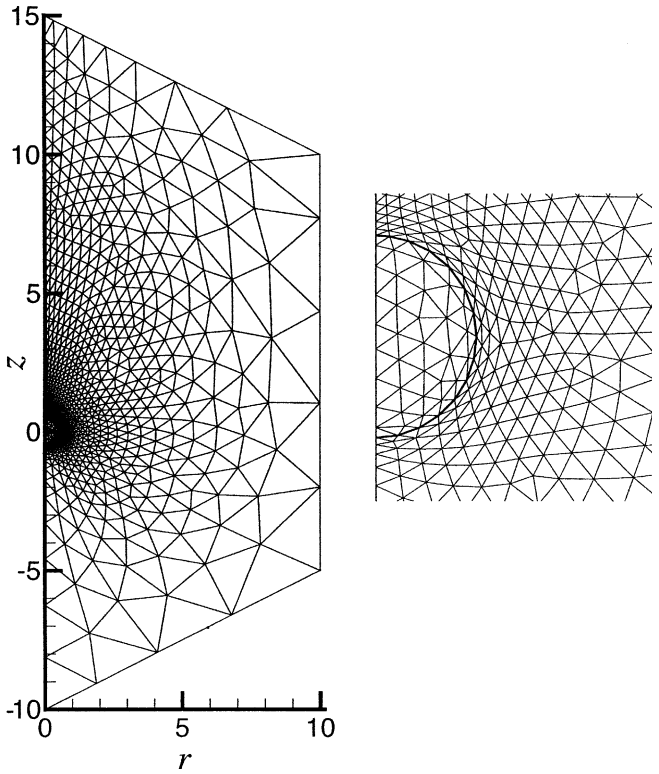

Fig. 1. Typical element mesh used for drop calculations with an insert of the region around the drop. The units of both coordinates are drop diameters.

body force required to hold a drop at specified flow conditions could be found as part of the iteration process.

All of the results presented are calculated on a trapezoidal domain given by the r, z points (0,−10), (0,15), (10,7.5), and (10,12.5) with the drop positioned at $r, z = (0, 0)$ where the units are drop diameters. This is shown in Fig. 1 which is a typical element mesh used for the calculations. At the lower boundary of the domain an inflow condition is enforced with a dimensionless velocity of unity. At the right and upper boundaries, a zero-stress condition is enforced. At the center line axisymmetric conditions are enforced.

To validate the method, we perform calculations of flow over a solid sphere and a liquid drop. These validation results have previously been presented in Helenbrook (2001). Table 2 shows the

Table 2
Convergence results for C_D

N	$P = 1$	$P = 2$	$P = 4$
17	1.02453	1.12223	1.15807
33	1.05333	1.09602	1.09065
65	1.07068	1.09196	1.09127
129	–	–	1.09129

results obtained for the coefficient of drag on a solid sphere, C_D, at a Reynolds number of 100. In the table, N is the number of polynomial basis functions on the surface of the sphere (a measure of the numerical resolution) and P is the polynomial degree of the basis (a measure of the order of accuracy). The most accurate result is when $N = 129$ and $P = 4$. The results presented in this paper are calculated using the mesh shown in Fig. 1 and a polynomial degree of 2. This corresponds to the conditions $N = 33$ and $P = 2$. Because we are using quadratic polynomials on each element, the flow resolution is double that implied by the element mesh. Comparing the drag result for $N = 33$ and $P = 2$ to the result at $N = 129$ and $P = 4$, we see that there is a 0.4% change. Thus, the drag results should be accurate to within 1%. The drag result determined from the experimentally derived correlation of Clift et al. (1978) for $Re = 100$, is 1.087 which is within 0.4% of this result. (The experimental uncertainty is not given.)

To determine the influence of the boundary conditions, we perform a simulation with the downstream boundary between $(0, 21)$ and $(14.5, 13.8)$ and the upstream boundary between (0, -14) and (14.5, -6.7). The simulation is performed with $N = 129$ and $P = 4$ so that the effects of the boundary position are isolated from the spatial discretization error. The resulting C_D is 1.08956 which is a change of 0.2%. Thus, the error associated with the proximity of the far-field boundary conditions should also be less than 1%.

To check the accuracy for liquid drop calculations, we perform a convergence test for a quasi-steady deformed drop. The conditions are $\rho_L/\rho_G = 100$ and $\mu_L/\mu_G = 100$. The body force on the drop is determined as part of the iterative process such that the terminal Reynolds number based on the gas properties is 60. The terminal Weber number of the drop is 4.0. This case was previously calculated by Dandy and Leal (1989). On a mesh given by $N = 33$ and $P = 2$ which is typical for the results presented here, the drag is 1.713. On a mesh with $N = 65$ and $P = 4$, the drag is 1.702 which is a 0.6% change. Both results are within 3% of the drag value calculated by Dandy and Leal (1989) (which is less accurate). The calculated streamwise length of the drop was 0.768495 diameters (an oblate drop) versus 0.768452 on the finer mesh; a change of 0.005%.

6. Deformation response

We begin the analysis by categorizing the drop deformation response. Figs. 2–4 show extreme examples of the three most prevalent drop shapes: oblate, prolate, and dimpled. The left half of the figures show the gas-phase pressure. The right half of the figures show the streamlines. We note that in some cases, the streamlines get closer together in regions in which one would expect slower velocities. This seems to contradict conservation of mass. (The distance between the gas-phase streamline closest to $r = 0$ and the streamline defined by $r = 0$ and the drop surface is an example.) This is because the results are axisymmetric. As the streamlines move to larger r for a constant flow velocity they get closer together because of the $2\pi r$ area weighting.

Fig. 2 shows an oblate drop. This is typically what one expects based on knowledge of flow over a sphere. For gas flow over a sphere, there is a high-pressure zone at the leading and trailing edges and a low pressure zone near the equator. This can be seen in the figure. The peak pressure is at the leading edge with the minimum pressure on the equator and some pressure recovery at the rear of the drop. This pressure distribution tends to collapse the drop and cause the oblate shape shown in the figure.

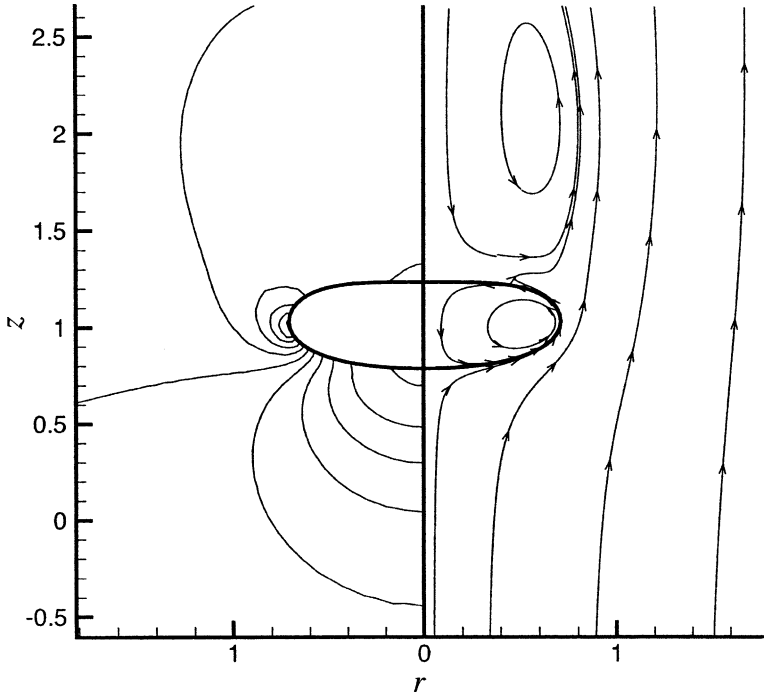

Fig. 2. Drop shape and dynamic pressure contours (left) and streamlines (right) for $\rho_L/\rho_G = 5$, $\mu_L/\mu_G = 10$, $We = 10$, and $Oh = 0.13$ ($Re = 110$). Pressure contours from leading stagnation point to minimum: 0.5 to -0.5 by -0.1.

Shown in the same figure is a large, separated recirculation zone in the gas at the rear of the drop. The appearance of a recirculation zone is primarily dependent on the Reynolds number of the calculation and is not limited strictly to the oblate drops; recirculation zones are also observed for prolate drops although they are less likely to form because of the streamlined shape. Calculations and experiments of flow over solid spheres have shown that a detectable recirculation zone appears at a Reynolds number of around 20 (Clift et al., 1978; Johnson and Patel, 1999). For drops, we find significant deviations from this result, depending on the liquid parameters. See Dandy and Leal (1989) for more information on the behavior of the recirculation zones.

Fig. 3 shows a prolate shape. This shape is opposite what one would expect based on the logic given above. The reason is that, as will be shown shortly, the deformation is caused by the liquid circulation rather than the gas flow. The recirculation pattern in the liquid (shown by the liquid-phase streamlines) causes high pressures in the interior of the drop at the leading and trailing edges. This, in turn, causes the drop to become prolate.

Fig. 4 shows a dimpled shape. This shape is defined by a concave region at the rear of the drop. In the figure, it appears as though there is a sharp corner at the rear of the drop, but this is because the radius of curvature in the dimple is 1/100 the radius of the drop. To resolve this curvature, the mesh resolution is much finer at the rear of the drop than that shown in Fig. 1. The gas-phase pressure in the region of the dimple is high as shown by the steep pressure gradients leading towards the dimple. This high pressure helps balance the surface tension stresses caused by the curvature in the dimple. We will show that this shape mainly occurs at low Reynolds numbers. In

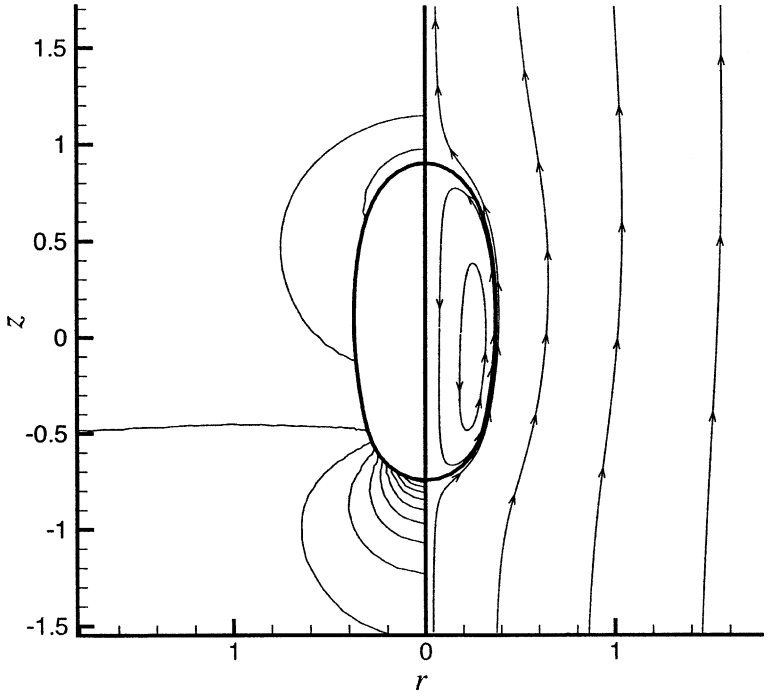

Fig. 3. Drop shape and gas-phase dynamic pressure contours (left) and streamlines (right) for $\rho_L/\rho_G = 500$, $\mu_L/\mu_G = 5$, $We = 5.0$, and $Oh = 0.04$ ($Re = 13$). Pressure contours from leading stagnation point to trailing minimum: 0.8 to -0.2 by -0.1.

most of the cases calculated, the dimple is less sharp such that the drop cross-section has a kidney-bean shape. Because the sharp dimple is such a peculiar shape, we have checked the result by increasing the distance of the boundary conditions. Moving the boundary conditions to 50 diameters, we find that the dimple actually becomes slightly sharper.

6.1. Oblate shapes

Of the above shapes, the prolate and oblate shapes are observed most frequently. We begin by determining the conditions that lead to the oblate shapes. Even for the rather extreme prolate and oblate examples shown in Figs. 2 and 3, the drop shapes remain fairly ellipsoidal. Excluding the dimpled shapes, only at Weber numbers larger than 10 is there significant deviation from ellipsoidal. Because of this, we use a single parameter, namely the aspect ratio, to describe the deformation. The aspect ratio E is defined as the ratio of the centerline height of the drop to the equatorial diameter.

We are interested in understanding and modeling how the drop shape changes as a function of conditions. To determine this, Fig. 5 shows one minus the aspect ratio for all of the cases calculated with an oblate shape. Since the drops are oblate, E is less than one and this is a positive number. Each curve on the figure corresponds to a calculation of increasing We at constant ρ_L/ρ_G, μ_L/μ_G, and Oh. The maximum We calculated for each curve is determined by several

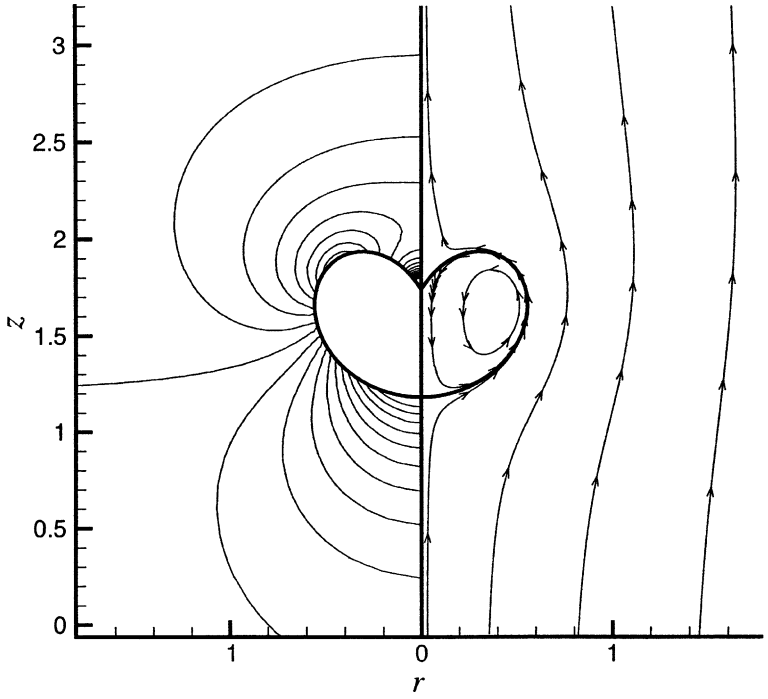

Fig. 4. Drop shape and dynamic pressure contours (left) and streamlines (right) for $\rho_L/\rho_G = 50$, $\mu_L/\mu_G = 15$, $We = 5.5$, and $Oh = 1.0$ ($Re = 5$). Pressure contours from leading stagnation point to minimum: 1.0 to -0.7 by -0.1.

different constraints. As discussed previously, for the small *Oh* cases, increasing the Weber number much past 1 causes the Reynolds number to exceed 200. For any constant *Oh* curve, if the Reynolds number exceeds 200 no further cases are calculated. For the larger *Oh* cases, there are two possible reasons for not going to higher *We*. The first is that we approach the critical Weber number of break-up beyond which there are no stable, steady solutions. The second is that the mesh becomes highly deformed such that a new mesh must be generated. This often occurs for the dimpled cases because of the high curvature in the dimple. In a few cases, we generate new meshes, but it is too time consuming to individually create new meshes for all of the different cases. We are currently working on an mesh adaptation algorithm to do this automatically.

We will not try to distinguish between the many curves on the figure but simply make some general observations. First, we notice that many of the cases seem to follow a similar power-law dependence on *We*. With increasing *We*, the drops become more oblate with a dependency which looks like $1 - E \sim We^{0.82}$. This line is shown on the figure for reference. The curves which branch off from this behavior towards negative values are cases that transition from an oblate to prolate shape. Based on the above discussion, we expect that the cause of this is pressure variation in the liquid. A simple estimate of the magnitude of these pressure variations can be obtained from the Hadamard–Rybczynski (H–R) solution for Stokes flow over a drop (Clift et al., 1978). The magnitude of the liquid velocity, U_L, is given by $U/(2 + \mu_L/\mu_G) \approx U\mu_G/\mu_L$ from which we can estimate the pressure variations due to convection as $\rho_L(U\mu_G/\mu_L)^2$ (From the H–R solution, we know that the pressure variations caused by the viscous forces do not lead to deformation).

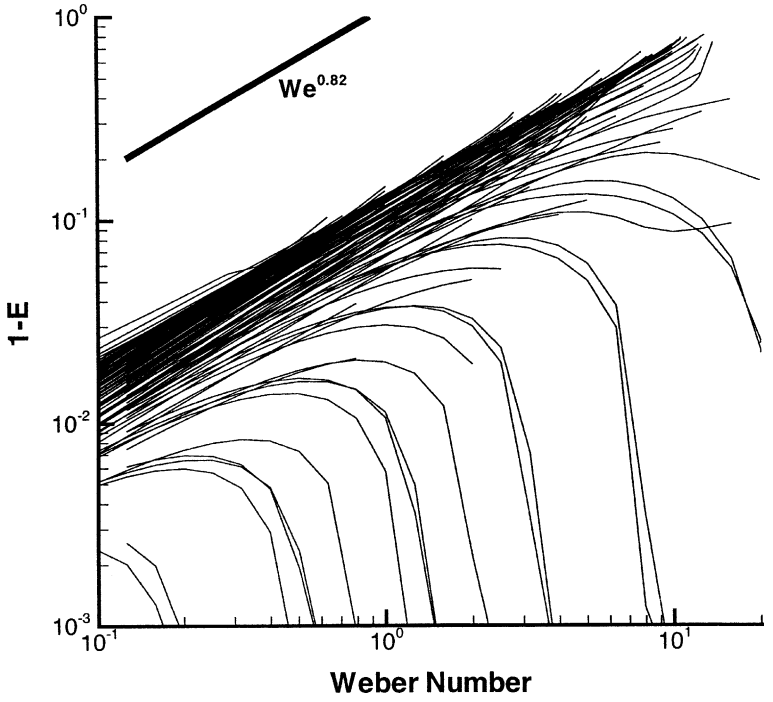

Fig. 5. Drop deformation for oblate drops. Conditions are listed in Table 1.

Although the velocity estimate is obtained from a Stokes flow solution, it does give a qualitative understanding of our results; cases with large density ratios and small viscosity ratios are more likely to be prolate. The curves that branch off correspond to conditions of $(\rho_L/\rho_G, \mu_L/\mu_G) = (500, 15)$, $(500, 10)$, $(50, 10)$, and $(50, 5)$. The largest density ratio and smallest viscosity ratio case (500,5) does not appear on the plot because all of the calculated points are prolate. This is consistent with this rough argument. We will examine the prolate cases in more detail in the following section.

Excluding the cases which transition to prolate, most of the results fall in a fairly narrow band around the curve $1 - E = 0.11We^{0.82}$. There is little variation with liquid properties between the cases $(5, 5)$, $(5, 10)$, $(5, 15)$, $(50, 15)$ because the deformation is mainly determined by the gas flow. There is, however, some weak sensitivity to the Ohnesorge number. The case $(\rho_L/\rho_G, \mu_L/\mu_G) = (5, 15)$ (which should have the least dependence on the liquid flow characteristics) varies from $(1 - E) = 0.078$ to 0.13 at $We = 1$ with Oh changing more than two orders of magnitude from 0.05 to 8.0. The most oblate drops correspond to those with the largest Oh.

It is interesting to note that since the Reynolds number is inversely proportional to the Ohnesorge number, $(Re = \sqrt{\rho_G/\rho_L}(\mu_L/\mu_G)\sqrt{We}/Oh)$, at constant We the most oblate drops have the smallest Reynolds number. This is somewhat counter intuitive since the H–R solution says there should be no deformation in a zero Reynolds number flow. However, the zero Reynolds number assumption in the H–R solution means that there are no convective effects and thus the analysis is also restricted to zero Weber number. When there is a finite Weber number, the

numerical results show that gas-phase viscous effects amplify the effects of convection in causing deformation.

6.2. Prolate shapes

The prolate shapes are caused by convection in the liquid. To isolate the deformation caused by the liquid from that caused by the gas, in Fig. 6, we plot $E-(1-0.11We^{0.82})$. This number is positive when the drops are elongated from the state we roughly expect based on gas-phase deformation alone. We only show the cases $(\rho_L/\rho_G, \mu_L/\mu_G) = (500, 5)$, $(500, 10)$, and $(50, 5)$ which are the cases that have the highest tendency to become prolate. Only every other *Oh* curve is shown to make the curves more visible. (*Oh* increases by a factor of $10^{0.4}$.) Much below 10^{-2} the results become meaningless because the deviation is smaller than the error in the simple curve fit to the gas-phase results.

Examining the figure, we see that deformation due to the liquid phase again follows a power-law dependence on the Weber number. In this case, the power is approximately 1.1 which is shown on the figure for reference. The dependence on the Weber number is greater than that for the oblate cases. This results in the transition seen in Fig. 5 between oblate at low *We* and prolate at higher Weber numbers. We also see that there is a much stronger dependence on the liquid

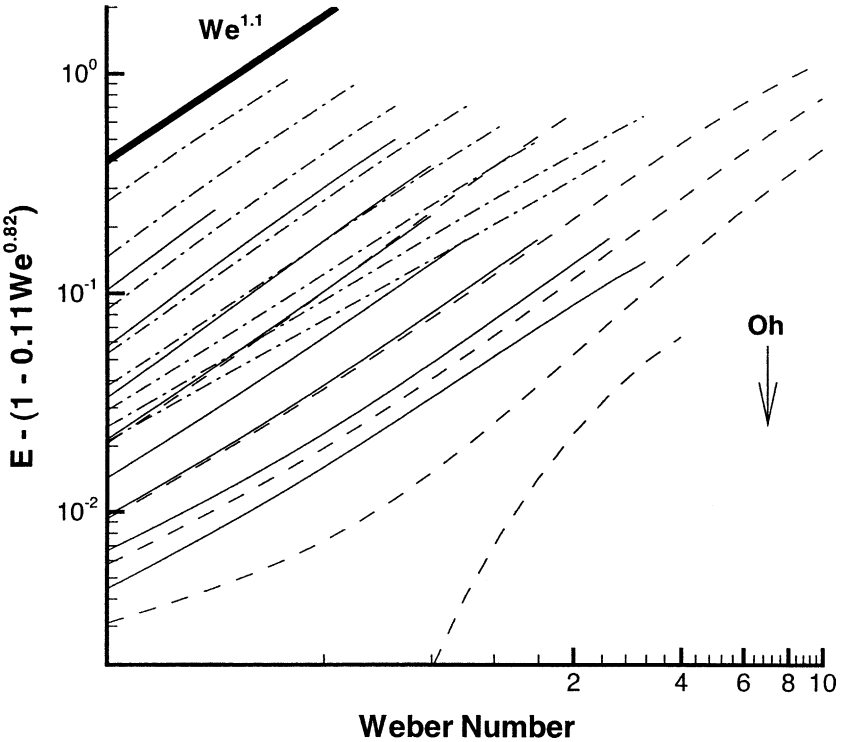

Fig. 6. Prolate drop deformation. Dash-dot lines: $(\rho_L/\rho_G, \mu_L/\mu_G) = (500, 5)$, $Oh = 0.00063$–0.4. Solid lines: $(500, 10)$, $Oh = 0.001$–0.63. Dashed lines: $(50, 5)$, $Oh = 0.005$–0.5. Oh curves increase by factors of $10^{0.4}$.

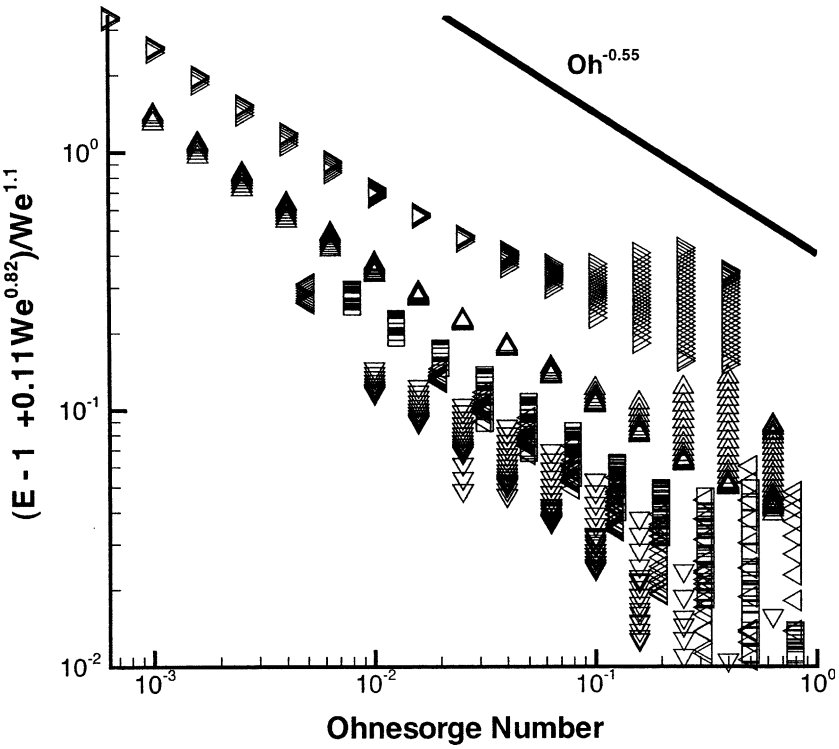

Fig. 7. Prolate drop deformation dependence on *Oh*. $(\rho_L/\rho_G, \mu_L/\mu_G)$ values: (▷) (500, 5); (Δ) (500, 10); (□) (500, 15); (◁) (50, 5); (▽) (50, 10).

properties and the Ohnesorge number for the prolate cases. The dependence on the liquid properties is expected based on the arguments given previously for the magnitude of the pressure variations in the liquid.

To quantify the dependency of the deformation on the Ohnesorge number, we divide the result shown in Fig. 6 by $We^{1.1}$ to eliminate the Weber number dependence and replot the results versus the Ohnesorge number. This is shown in Fig. 7. In this case, each curve of constant $\rho_L/\rho_G, \mu_L/\mu_G$ and *Oh* at varying Weber number is a vertical line. If we do a good job eliminating the dependence on *We*, we should get nearly a point for each curve. As was the case previously, the scatter increases at lower values of the deformation. There is also increased scatter for larger values of *Oh* because, as we will show in the next section, the drops become dimpled under these conditions. The five cases which exhibit prolate shapes are shown, $(\rho_L/\rho_G) = (500, 5)$, $(500, 10)$, $(500, 15)$, $(50, 5)$, $(50, 10)$, and $(5, 5)$. From the figure we can see that dependence on the Ohnesorge number can be modeled as $Oh^{-0.55}$. Thus when the fluid properties are held fixed, smaller Ohnesorge numbers (larger drops) have a greater tendency to become prolate.

To finish the modeling of the deformation caused by the liquid phase, we need to determine the dependence on the liquid properties. Based on the ratio of the convective effects in the gas to the surface tension stress, $\rho_L U_l^2 d/\sigma \approx \rho_L/\rho_G(\mu_G/\mu_L)^2 We$, we expect that the parameter $\rho_L/\rho_G(\mu_G/\mu_L)^2$ will be important. Going through the process of eliminating the *Oh* dependence and plotting

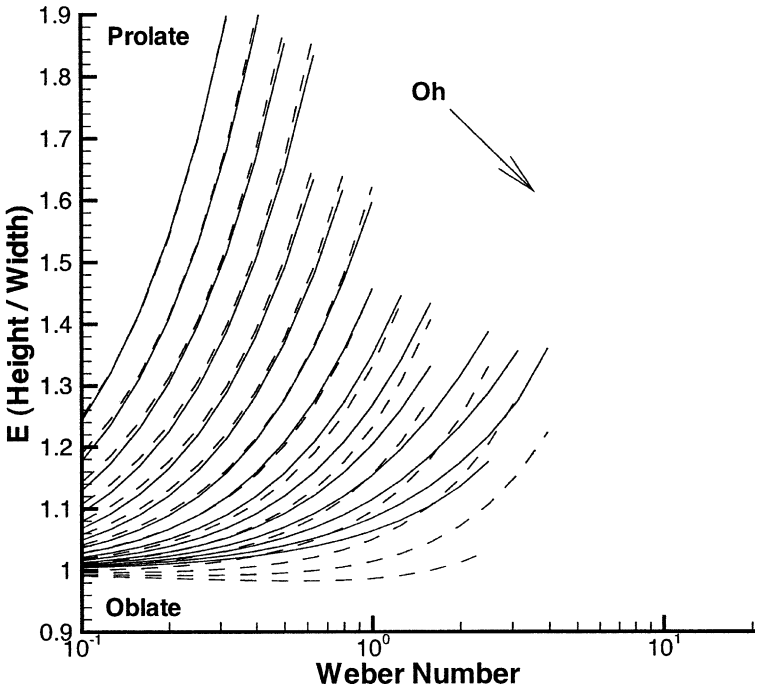

Fig. 8. Drop deformation for $\rho_L/\rho_G = 500$, $\mu_L/\mu_G = 5$, and $Oh = 0.00063$–0.40 ($0.00063 \times 10^{2.8}$) by factors of $10^{0.2}$. Solid lines–numerical results, dashed lines–correlation.

the results versus this parameter, we find that there is again a good collapse of the data. A correlation predicting the deformation can then be determined to be

$$E = 1 - 0.11We^{0.82} + 0.013\sqrt{\frac{\rho_L}{\rho_G}}\frac{\mu_G}{\mu_L}Oh^{0.55}We^{1.1} \tag{1}$$

which shows the dependence on the liquid-phase parameters. This dependence is as expected; increased liquid density and decreased viscosity result in a more prolate drop shape. We note that there have been several previous attempts to model the drop shape response such as those by Taylor and Acrivos (1964), Clift et al. (1978), and Grace and Wairegi (1992), but none of these models give quantitative results for the range of conditions studied here nor do they predict the dependence on the liquid parameters seen in our calculations.

To validate this correlation, Figs. 8 and 9 show the calculated aspect ratio of the drops as a function of Weber number for $\rho_L/\rho_G, \mu_L/\mu_G = (500, 5)$ and $(5, 15)$ respectively. In the first case, the deformation is primarily determined by the liquid phase while in the second it is determined by the gas phase. *Oh* increases crossing curves moving from the top to the bottom of the plots. The *Oh* range for each figure is given in the captions. The solid lines on the figures are the computed results and the dashed lines are the algebraic correlation. For all of the cases we have calculated, the agreement between the correlation and the computed results is as good or better than that shown in these two figures. For the prolate case shown, there is deviation at large *Oh*, but this is

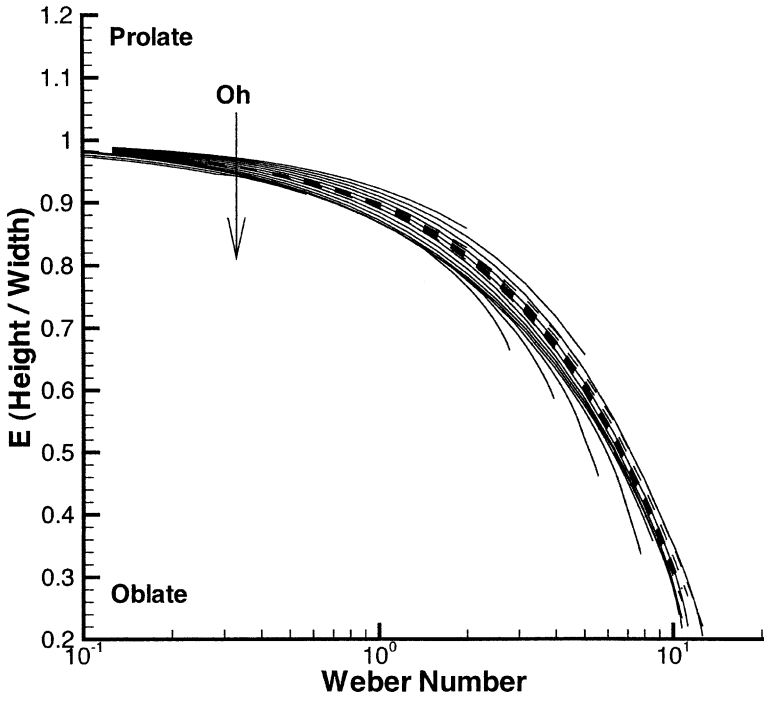

Fig. 9. Drop deformation for $\rho_L/\rho_G = 5$, $\mu_L/\mu_G = 15$, and $Oh = 0.05$–20 ($0.05 \times 10^{2.6}$) by factors of $10^{0.2}$. Solid lines–numerical results, dashed lines–correlation.

not consistent across all of the cases. As expected, the oblate cases do not capture the weak variation in deformation with *Oh*.

Examining Fig. 8, we see solutions with aspect ratios approaching two. This leads us to question the validity of the axisymmetric assumption. Simple experiments with falling solid ellipsoids have shown that ellipsoids tend to align themselves with the largest cross-sectional area normal to the flow (Clift et al., 1978). Thus, we suspect that the prolate cases are not axisymmetrically stable but rather will tumble in a three-dimensional fashion as they move through the gas. This may explain why prolate falling drops have never been reported even in uncontaminated experiments while wobbling or oscillating drops have been reported (Clift et al., 1978; Hsiang and Faeth, 1992).

To determine an expression for the onset of this proposed tumbling instability, we set $E = 1$ in Eq. (1) and substitute the relation for the Weber number as a function of *Oh* and *Re*.

$$Re \approx 70\left(\frac{\rho_G}{\rho_L}\right)^{3/2}\left(\frac{\mu_L}{\mu_G}\right)^{3} \tag{2}$$

To obtain this result, in Eq. (1) we change the power of the *Oh* term to -0.5, and the difference in the power of the two Weber number terms is rounded to 0.25. This equation predicts that for a given set of fluid properties, the crossover point from oblate to prolate is at a fixed Reynolds number. To verify this, in Fig. 10 we plot the results for $\rho_L/\rho_G = 500$ and $\mu_L/\mu_G = 15$ with the Reynolds number on the horizontal axis. The figure confirms that the oblate to prolate transition

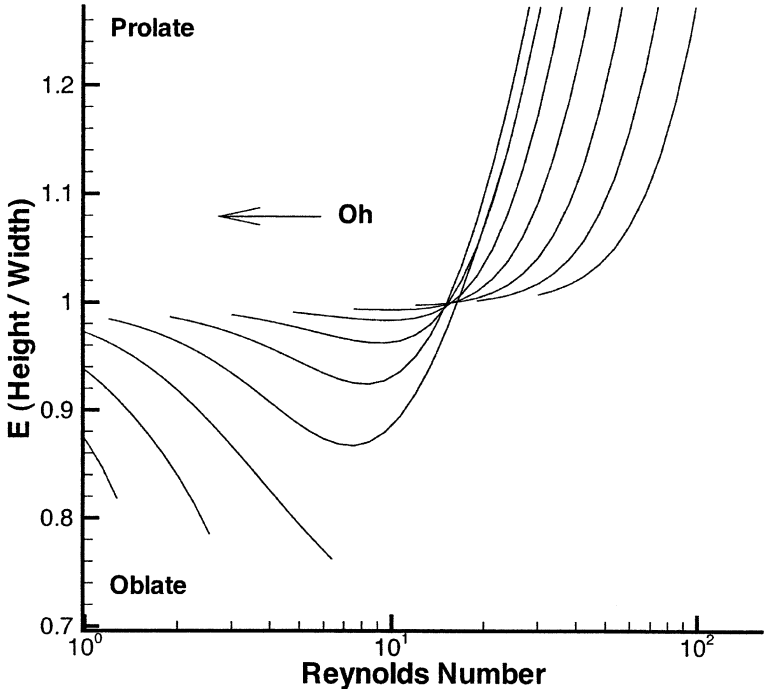

Fig. 10. Drop deformation for $\rho_L/\rho_G = 500$, $\mu_L/\mu_G = 15$, and $Oh = 0.008$–2.0 ($0.008 \times 10^{2.0}$) by factors of $10^{0.2}$.

occurs at a fixed Reynolds number. The above equation predicts that transition will occur at $Re = 21$ while in the figure the crossover is near $Re = 15$. If we examine the other cases which transition from oblate to prolate, we find that the crossover again occurs at a single Reynolds number. For $(\rho_L/\rho_G, \mu_L/\mu_G) = (50, 5)$, $(50, 10)$, $(500, 10)$, and $(500, 15)$ the crossover occurs at $Re = 25$, 130, 4.8, and 15 respectively while the above equation predicts 25, 196, 6.2, and 21.

Experimental results on an oscillatory drop regime usually predict the transition as a line of constant Weber number rather than constant Reynolds number (Hsiang and Faeth, 1992). This may be because the shape oscillations only become noticeable when the Weber number is fairly large. Another difference is that the transition is predicted to exist independent of the liquid and gas fluid properties. This does not agree with our predictions. This may be because three-dimensional perturbations which are always present in an experiment obscure the transition. Another possibility is that surface contaminants may be affecting the experiment. There is evidence that surface contaminants tend to reduce the magnitude of internal circulation in a drop (Clift et al., 1978). This will reduce the tendency for drops to become prolate and thus either eliminate or alter the conditions which cause a transition to oscillation. We have performed some preliminary calculations with a contaminant model and found that the internal circulation pattern is radically different. In some cases, this causes the drop shape to change from prolate when uncontaminated to oblate when contaminated. Thus, the three-dimensional instability may be only observable in contaminant-free experiments.

It has been suggested that contaminated drops can be modeled as a drop with zero internal circulation (Haywood et al., 1994). If this is true, then the low-density-ratio, high-viscosity-ratio

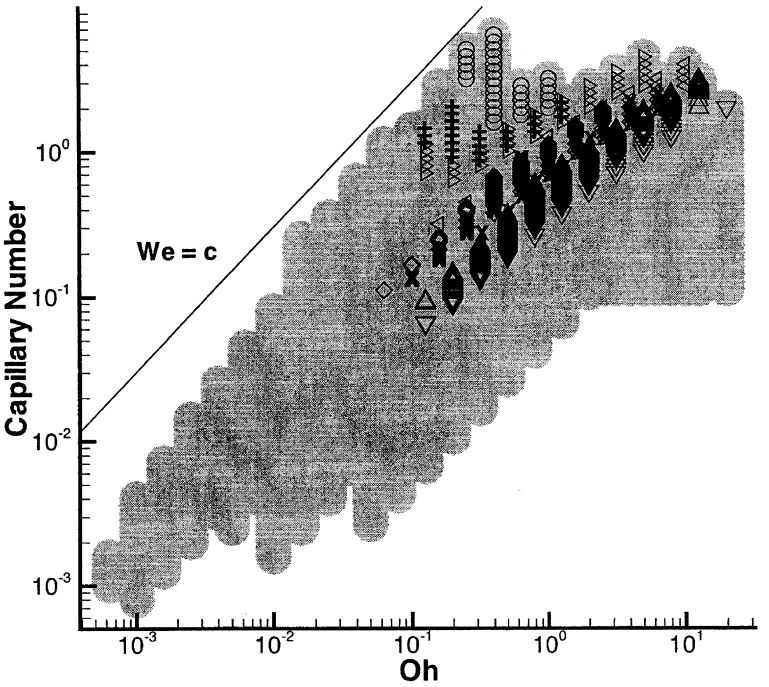

Fig. 11. Capillary number of drops with dimpled shape. Density, viscosity ratio: (∇) 5, 15; ($\diamond$) 50, 15; (+) 500, 15; (Δ) 5, 10; ($\triangleleft$) 50, 10; ($\circ$) 500, 10; ($\times$) 5, 5; ($\triangleright$) 50, 5; None 500, 5.

results should behave similarly to contaminated drops. In this case, we can neglect the deformation caused by the liquid. In Eq. (1), we then only have a dependence on the Weber number and a very simple model for deformation. The accuracy of this approximation needs to be determined, however it does give a rough estimate of the possible effects of contaminants on deformation.

6.3. Dimpled shapes

The dimpling phenomenon is primarily due to gas-phase viscous effects and occurs when the Capillary number, $Ca = \mu_G U/\sigma = We/Re$ is O(1) or larger. To confirm this, in Fig. 11 we plot the Capillary number versus Ohnesorge number of all the points that have a dimpled shape with a dark symbol. For reference, the gray background area is the domain over which we have performed calculations. A line of constant Weber number is also shown on the plot, this is determined by $Ca = \sqrt{We}\,Oh(\mu_G/\mu_L)\sqrt{\rho_L/\rho_G}$. The equation for the line is actually $Ca = 30\,Oh$. The actual value of the Weber number on the line depends on the gas and liquid properties. There are no calculations above this line because these conditions exceed the critical Weber number for breakup. The first thing we see from this figure is that the dimpled shapes occur when the Capillary number is O(1) in magnitude. If we examine each density and viscosity ratio case separately, we find that, independent of the liquid properties, all of the cases show dimpling when Ca is O(1) except for $\rho_L/\rho_G = 500$, $\mu_L/\mu_G = 5$ which never becomes dimpled. Thus, the liquid properties are

not a primary factor in the appearance of dimpling. This confirms our original statement that the phenomenon is due to gas-phase viscous effects.

Although dimpling is primarily a gas-phase effect, there is a sensitivity to the liquid parameters. In the figure, there are two distinct trends in the appearance of dimpling: one showing $Ca \approx 1$ over a range of Oh, and the other showing an increase in Ca number from 0.1 to 1.0 with Oh. The first trend occurs for the cases, $(\rho_L/\rho_G, \mu_L/\mu_G) = (500, 15)$, $(500, 10)$, and $(50, 5)$. We also include the case $(500, 5)$ which does not develop dimpled shapes in this group. For these conditions, the liquid circulation has a strong effect on the deformation. This causes the drops to become prolate which increases the curvature at the rear of the drop and opposes dimpling. Because of this, the Capillary number must be approximately one, independent of Oh, for dimpling to occur. The remaining cases tend to become oblate with increasing Weber number. This flattens the back of the drop and makes it easier for a concave region at the rear of the drop to form. For these cases, the Capillary number at which dimpling occurs increases with Oh from 0.1 to 1.0.

Although dimpling occurs when Ca is O(1) in the above results, we know from the H–R solution that if convective effects are ignored completely a spherical drop does not deform at any Capillary number. Thus, the dimpling effect must be a combined effect of both convection and diffusion. In the limit of low Reynolds numbers, we expect the onset of dimpling to be somewhere between the lines $Ca = O(1)$ and $We = O(1)$. This is in agreement with our previous conclusion that gas-phase viscosity tends to increase the drop deformation. Both of the trends shown fall between the two limits $We = O(1)$ and $Ca = O(1)$, however because the lowest Reynolds number for any of the cases is 0.1, the results cannot be used to extrapolate to the low Reynolds number limit.

Performing calculations at Reynolds numbers lower than 0.1, we find that there is a strong dependence of the deformation on the position and type of far-field boundary conditions used. Moving the boundaries to 25 diameters does not eliminate this dependence. Since high Capillary number drops do not occur in most spray devices, we do not pursue this limit further. We note that the prediction that deformation will occur between $Ca = O(1)$ and $We = O(1)$ is in agreement with analytic predictions in this limit. Examining the analytic solution of Taylor and Acrivos (1964) which is a perturbation analysis for small We and Re, we see that they predict deformation to be of the form

$$E = 1 + f(\mu_L/\mu_G, \rho_L/\rho_G)We + g(\mu_L/\mu_G, \rho_L/\rho_G)We\,Ca \tag{3}$$

where f and g are algebraic functions. When the Capillary number is large, the last term dominates and deformation occurs when $We\,Ca$ is O(1). This falls between $Ca = O(1)$ and $We = O(1)$.

Stokes flow calculations of viscous drops have shown that a perturbed spherical drop has a tendency to form a sharp dimple at the rear of the drop (Stone, 1994). This further confirms that this is a low Reynolds number effect. The Stokes flow calculations show drops with a narrow and deep dimple at the rear. For large Oh values such as that shown in Fig. 4, we also find fairly narrow dimples. For smaller values of Oh, our results have a broad dimple at the rear of the drop. This transition is expected since decreasing Oh at constant Ca corresponds to a larger Reynolds number flow. When $Oh < (\mu_L/\mu_G)\sqrt{\rho_G/\rho_L}$, the Capillary number is less than one when the Weber number is one. Under these conditions, the drops are either prolate or oblate and do not dimple because viscous effects are less significant.

Another comment about dimpling is that, since the Ohnesorge must be O(1) or larger for the phenomenon to occur, dimpled shapes are more likely to be observed for falling drops than for injected drops. As discussed in the time scale analysis section, when the Ohnesorge number is large, the velocity of an injected drop decays more rapidly than the drop can deform. Thus, the drop will not have time to reach its quasi-steady deformed state. Drops under a body force have an infinite amount of time to deform and thus can evolve to a dimpled state.

The effect of dimpling can be seen in plots of aspect ratio versus Weber number such as Fig. 9. For oblate cases, the large *Oh* curves decrease faster than the approximate $1 - We^{0.82}$ correlation near the higher Weber number end of the curves. This drop below the $1 - We^{0.82}$ correlation curve is caused by the formation of a dimple at the rear of the drop which decreases its centerline height. Because the formation of a sharp dimple causes large mesh deformation, the calculations are not continued much past the dimple's initial formation.

From the above discussion, we have good confidence that we can estimate the drop shape given the flow conditions. The deformation correlation given by Eq. (1) can be used to predict drop shapes for conditions $Oh < (\mu_L/\mu_G)\sqrt{\rho_G/\rho_L}$ with reasonable accuracy. Above this value the drop shape will become dimpled which is not included in the correlation. The Weber number can range from 0 to approximately 10. Above $We = 10$, the drop approaches the critical value and it is difficult to predict its behavior.

7. Drag

Given the deformation information, we now examine the drag response of a drop. The drag on a viscous liquid drop is usually modeled by a drag law for a solid sphere. There are two effects which can cause the liquid-drop drag to deviate from that of a solid sphere. These are internal circulation and the deviation of the drop from a spherical shape. In the following, we examine both of these effects.

In Figs. 12–14 we plot, as a function of Reynolds number, the percentage deviation in drag from that of a solid sphere with the same volume. Figs. 12 and 13 are at the same density ratio, 5, but different viscosity ratios, 5 and 15. Fig. 14 is at the same viscosity ratio as Fig. 13, namely 15, but different density ratio, 500. The baseline solid-sphere drag at any Reynolds number is calculated using the same gas-phase mesh and boundary conditions as used for the drop calculations. Each solid curve corresponds to a constant Ohnesorge number calculation. The largest *Oh* cases are at the left side of the plots. The initial point of each curve is at $We = 0.1$ or less. The Weber number increases quadratically with the Reynolds number along the curves. The scale of the axis is the same for each plot although the origin is shifted vertically depending on the case. The thick curve and the dashed curves are algebraic correlations which will be discussed shortly.

7.1. Internal circulation

We begin by examining the effect of internal circulation on the drag. In the low Weber number limit, the drop is spherical, and internal circulation is the primary cause for the change in the drag.

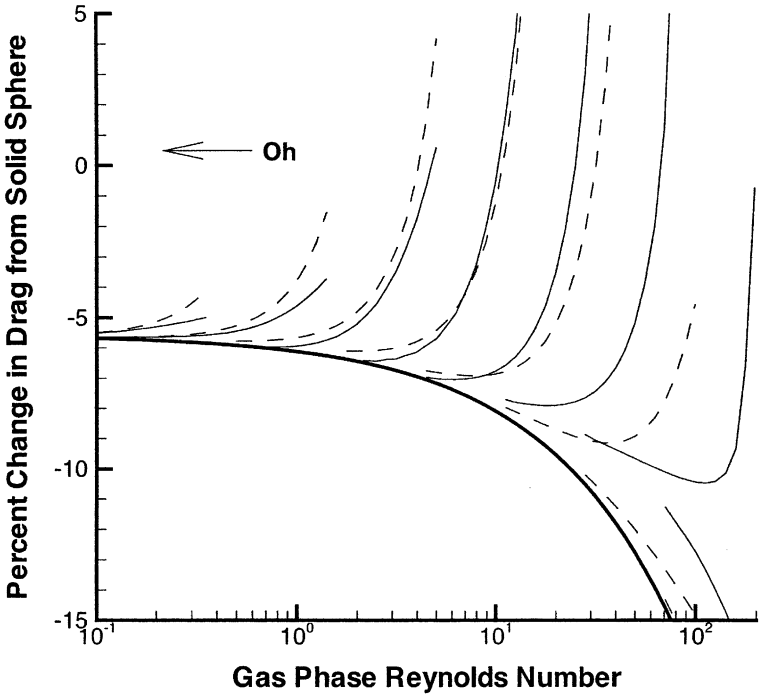

Fig. 12. Drag deviation from a solid sphere for $\rho_L/\rho_G = 5$, $\mu_L/\mu_G = 5$, and $Oh = 0.01$–6.3 ($0.01 \times 10^{2.8}$) by factors of $10^{0.4}$. Solid lines–numerical results, Thick solid line–internal circulation correlation, Dashed lines–total correlation.

For each constant *Oh* curve, the low Weber number limit is approximated by the lowest Reynolds number points on the curve since $We = 0.1$ or less for these points. Under these conditions, the surface tension is an unimportant parameter since the drops are nearly spherical. The primary parameters which can affect the drag are then ρ_L/ρ_G, μ_L/μ_G and *Re*. All of the numerical curves on a single plot should collapse to a single curve at low Weber numbers. Examining the figures, we see that this appears to be the general trend. If we were to start the calculations at lower We, this trend would be even more apparent. This single curve represents the effects of internal circulation on a spherical drop.

In the low Reynolds number limit, the H–R solution predicts that the percentage change is $-100/(3 + 3\mu_L/\mu_G)$. For the reader's reference, the thick solid curves shown on the figure, which will be described at the end of this section, reproduce this result in the low Reynolds number limit. At low Reynolds and Weber number, the numerical curves should all converge to this analytic result. Examining the figures at low Reynolds numbers, we see good agreement with the analytic result with a maximum difference of less than 1/2 of a percent. This gives us further confidence in the numerical results.

In the low Reynolds number limit, the density ratio should not have an effect on the drag because the convective term is negligible; this is the only term in which the density appears. Comparing the low *We* drag curves between Figs. 13 and 14 shows that this is true of our results even at larger Reynolds numbers. To facilitate this comparison, note that the thick solid curves

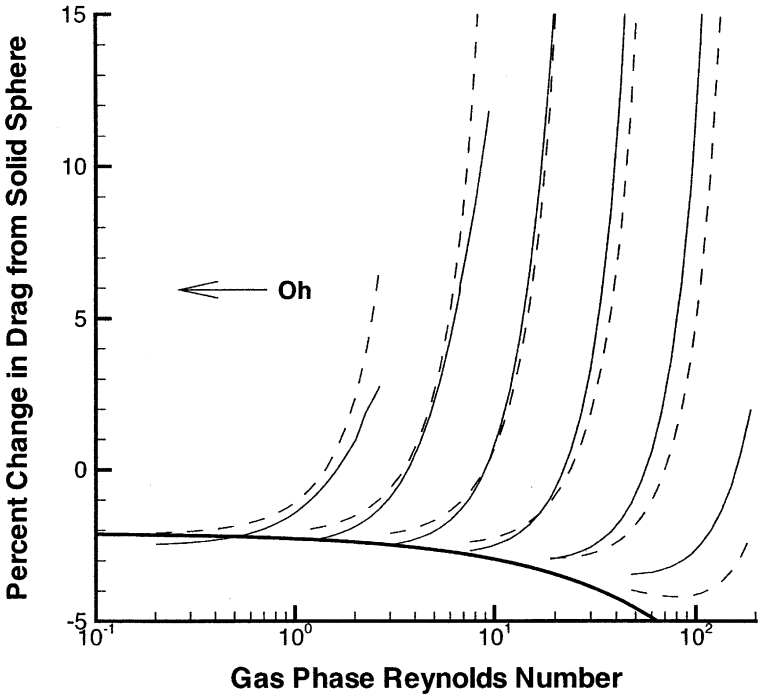

Fig. 13. Drag deviation from a solid sphere for $\rho_L/\rho_G = 5$, $\mu_L/\mu_G = 15$, and $Oh = 0.05$–12.6 ($0.05 \times 10^{2.4}$) by factors of $10^{0.4}$. Solid lines–numerical results, Thick solid line–internal circulation correlation, Dashed lines–total correlation.

are the same on both plots. From this we can say that the density ratio is not an important parameter when modeling the effect of internal circulation on drag for *Re* up to 200.

The reason for this independence is given by Rivkind and Ryskin (1976). They explain that in low *Re* flow, the liquid flow is a Hill's spherical vortex (Hill, 1894) and that this is a solution of the Navier–Stokes equations independent of the liquid-phase Reynolds number, $Re_L = \rho_L U_L d/\mu_L$. Variations in ρ_L are therefore irrelevant if the gas-phase Reynolds number is low. They are also irrelevant if the liquid-phase Reynolds number is low because the liquid convective term is negligible. $Re \gg 1$ and $Re_L \gg 1$ is then the only region in which the density ratio may have a strong effect. Examining all of our results, for which in some cases Re_L approaches 4000, we find that this is not the case. Thus, the density ratio is unimportant when examining the effect of internal circulation on drag. This conclusion has been made in several previous studies of the flow around liquid drops with an assumed spherical shape (Rivkind and Ryskin, 1976; Oliver and Chung, 1987).

Although Hill's spherical vortex is a solution to the Navier–Stokes equations at all Reynolds numbers, the normal stress on the interior of the drop surface changes as a function of Reynolds number. This is the reason that ρ_L is important in determining the drop shape. For drag in the low Weber number limit however, only the surface velocity distribution and tangential stresses are important since the drop is constrained to be nearly spherical by the surface tension. These are both independent of the liquid density.

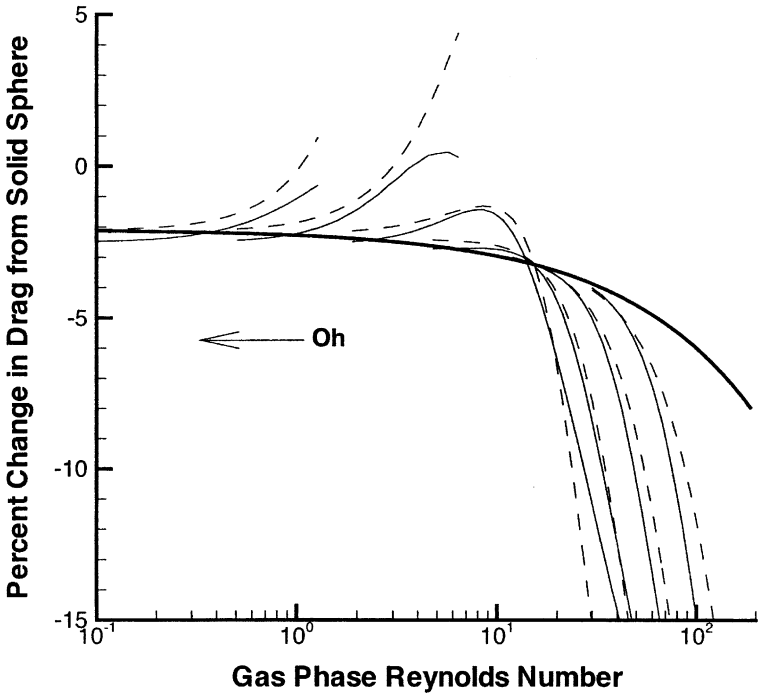

Fig. 14. Drag deviation from a solid sphere for $\rho_L/\rho_G = 500$, $\mu_L/\mu_G = 15$, and $Oh = 0.008$–2.0 ($0.008 \times 10^{2.4}$) by factors of $10^{0.4}$. Solid lines–numerical results, Thick solid line–internal circulation correlation, Dashed lines–total correlation.

The only parameters needed to model the effect of internal circulation are then Re and μ_L/μ_G. Rivkind and Ryskin (1976) and Oliver and Chung (1987) have proposed algebraic correlations which depend only on Re and μ_L/μ_G to describe the drag over a spherical liquid drop. We have examined these correlations in relation to our numerical results. To analyze the behaviors, we examine the percentage change in the drag from that given by the correlation for a solid sphere. This isolates the internal circulation effect and makes the results less dependent on the actual solid-sphere drag law used.

The correlation of Rivkind and Ryskin does not reproduce the Stokes flow result; as the Reynolds number approaches zero, the error approaches infinity. In the range $20 < Re < 100$, which was suggested by Oliver and Chung for its use, we find that it produces qualitatively incorrect results compared to our numerical results. The reason for this is probably that Oliver and Chung only looked at the total drag rather than the percentage change in drag. Since the solid-sphere drag correlation Rivkind and Ryskin used is fairly accurate in this range, their results appear to be accurate. In fact, for most conditions the percent correction does not fall in the range shown on Figs. 12–14.

The drag correlation proposed by Oliver and Chung (1987) is limited because the solid-sphere drag correlation they used is only accurate for small Re. Modifying their correlation with a more accurate solid sphere drag correlation, we find that the results predict the correct trends for Re up to 100 and also agree with the analytic result for small Re. However, the decrease in drag at higher

Re shown in Figs. 12–14 is under predicted. This is probably because we are using the correlation in a range outside of its intended use. Because of these limitations, we have created the following correlation for the effect of internal circulation on drag

$$\frac{D_{\text{drop}}}{D_{\text{solid}}} = \left(\frac{2+3\mu_{\text{L}}/\mu_{\text{G}}}{3+3\mu_{\text{L}}/\mu_{\text{G}}}\right)(1-0.03(\mu_{\text{G}}/\mu_{\text{L}})Re^{0.65}) \tag{4}$$

where D_{drop} and D_{solid} are the drag forces on a spherical drop and a solid-sphere respectively. This correlation defines the thick solid curves shown in Figs. 12–14. In the low *Re* limit, the above correlation reproduces the analytic result. As can be seen from the figures, this correlation also accurately predicts the effect of internal circulation at higher Reynolds number. Because only three viscosity ratios are studied, the dependence of the coefficient of the *Re* term on viscosity ratio is not well established and may be inaccurate on extrapolation to viscosity ratios outside this range (especially lower viscosity ratios). At high-viscosity-ratios, the correction approaches unity because internal circulation effects become negligible.

7.2. Deformation effect

To complete the modeling of drag for a liquid drop, we consider the effect of deformation. As can be seen in the figures, the deviation of the drag from that of a liquid sphere follows the aspect ratio of the drop. Prolate drops tend to show a decrease in the drag below the internal circulation curve due to their decreased frontal area. For cases which transition from oblate to prolate such as $(\rho_{\text{L}}/\rho_{\text{G}}, \mu_{\text{L}}/\mu_{\text{G}}) = (500, 15)$ the transition point in drag above and below the internal circulation curve is approximately at a constant *Re*, consistent with Eq. (2). This can be seen in Fig. 14. Oblate cases such as $(\rho_{\text{L}}/\rho_{\text{G}}, \mu_{\text{L}}/\mu_{\text{G}}) = (5, 5)$ and (5,15) (Figs. 12 and 13) show an increase in drag due to their increased frontal area. The magnitude of these effects is not fully shown by the figures; we have restricted the range of the vertical axis to 20% to show the details of the internal circulation effect. The deviations due to deformation can be much larger. The maximum deviation for the prolate cases occurs for $\rho_{\text{L}}/\rho_{\text{G}} = 500$ and $\mu_{\text{L}}/\mu_{\text{G}} = 5$ and is -35%. The maximum deviation for the oblate cases occurs for $\rho_{\text{L}}/\rho_{\text{G}} = 5$ and $\mu_{\text{L}}/\mu_{\text{G}} = 15$ and is a 115% increase in the drag force.

To model the effect of deformation on drag, we follow the procedure suggested by Clift et al. (1978). First, the drag on a sphere of equivalent equatorial diameter to the drop is calculated using a solid-sphere drag correlation. Assuming the drops are perfect ellipsoids, the equatorial diameter is given by $dE^{-1/3}$. The Reynolds number of the sphere with the equivalent equatorial diameter, Re_{ed}, is then given by $ReE^{-1/3}$. Using the definition of C_{D}, we arrive at the following for the drag

$$D = \frac{1}{2}\rho_{\text{G}}U^2 A_{\text{ed}} C_{D_{\text{ed}}} = \frac{1}{8}\rho_{\text{G}}U^2\pi d^2 E^{-2/3} C_{D_{\text{ed}}} \tag{5}$$

where $C_{D_{\text{ed}}}$ is the coefficient of drag calculated from a solid sphere drag correlation at Re_{ed}. In the second equation we have substituted $\pi d^2 E^{-2/3}/4$ for A_{ed}, the cross-sectional area of the ellipsoid. This gives the drag for a sphere of equivalent equatorial diameter as the ellipsoid. To calculate the drag on the ellipsoid, this drag force is then multiplied by the drag ratio between a sphere and an

ellipsoid of the same equatorial diameter. There is no analytic expression for this valid at all Reynolds numbers, however Clift et al. suggest that the low Reynolds number result can be used over the entire range of Re. This is approximated by $0.2(4+E)$ which in Stokes flow is accurate to within 6% for $0 < E < 2.0$ (Clift et al., 1978). Multiplying by this expression gives us the drag on a solid ellipsoid. To incorporate the effect of internal circulation in the drop, this drag is then multiplied by the correction given in Eq. (4).

The dashed lines shown in Figs. 12–14 are calculated using the above procedure. The aspect ratio is determined using Eq. (1). The baseline solid-sphere drag correlation used is given by

$$C_D = \frac{24}{Re}[1 + 0.1935 Re^{0.6305}] \tag{6}$$

which is the correlation suggested by Clift et al. (1978) to be appropriate for the range $20 \leqslant Re \leqslant 260$. Because we plot the correction to the solid-sphere drag, the curves are fairly insensitive to the exact form of the correlation.

The above drag modeling procedure does a reasonable job of predicting the dependence of the drag on the aspect ratio. However, we do notice some consistent differences between the modeled results and the numerical results for all of the cases. The first is that in the range $0.1 < Re < 5$, the drag model consistently over predicts the sensitivity of the drag to aspect ratio. This is unexpected since in the low Reynolds number limit, the drag model should give better results. To determine whether the cause of this inaccuracy is the prediction of the aspect ratio of the drop, we recalculate the drag model curves using the aspect ratio determined directly from the simulations. The results of these calculations are very similar to those based on the aspect ratio correlation. From this we conclude that the over prediction is caused by the drag modeling not the aspect ratio correlation. Further work is needed to determine the source of this inaccuracy.

Another consistent trend is that at higher Reynolds numbers, the drag sensitivity to deformation is under predicted. However, as verified by recalculating the results using the numerically determined aspect ratio, most of the under prediction is due to the drag model. Since we are unsure of the source of the inaccuracy in the low Re limit, we will refrain from speculating on the reasons for this under sensitivity in the high Re limit.

Overall, the drag model seems to provide an accurate prediction of drag on deforming liquid drops. For most of the cases calculated, the correction is within 5% of the numerical values. For highly deformed cases, the accuracy degrades slightly. For our most extreme case of drag increase, $\rho_L/\rho_G = 5$, $\mu_L/\mu_G = 15$, the drag increases 115% and the model predicts an increase of 85% which, although low, is still a reasonable prediction. The worst case is for $\rho_L/\rho_G = 5$, $\mu_L/\mu_G = 5$ shown in Fig. 12. For the curve that reaches the top of the figure at $Re = 100$, the maximum drag increase is 50%. The model under predicts this significantly because of the combined facts that the deformation is under predicted and the drag sensitivity to the deformation is also under predicted.

An alternative to the above model is a drag correlation developed by Haywood et al. (1994). Their correlation is not based on the deformation but directly models the drag as a function of Weber number and Reynolds number. This correlation is given by

$$D = \frac{1}{8}\rho_G U^2 \pi d^2 C_{D_{\text{solid}}}(1 + 0.06 Re^{-0.12} We^{1.4}) \tag{7}$$

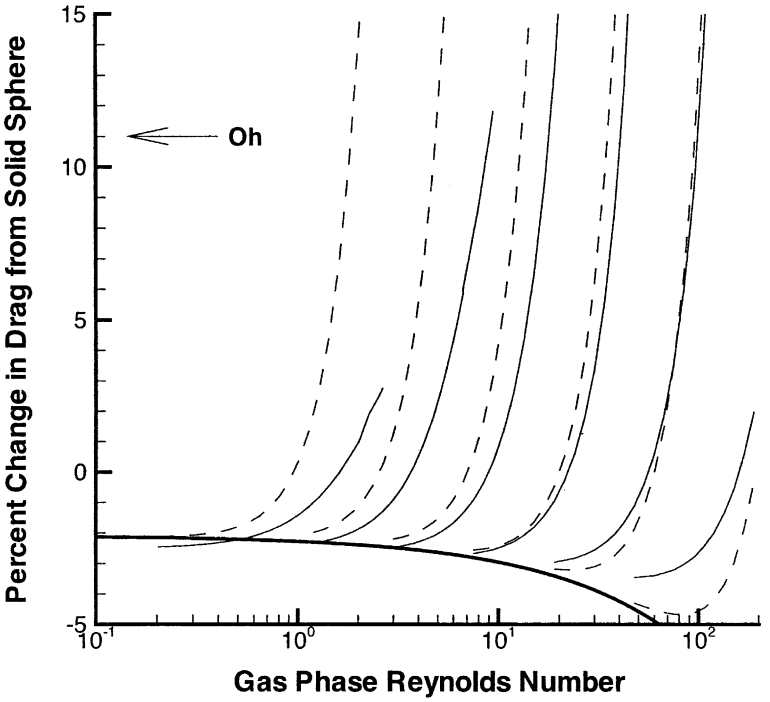

Fig. 15. Comparison between numerical results and the drag correlation of Haywood et al. (1994) for $\rho_L/\rho_G = 5$, $\mu_L/\mu_G = 15$, and $Oh = 0.05$–12.6 ($0.05 \times 10^{2.4}$) by factors of $10^{0.4}$. Solid lines–numerical results, Dashed lines–correlation of Haywood et al. (1994).

The correlation was derived from simulations in which all liquid motion was suppressed, thus this result will only be valid for conditions under which the liquid motion is unimportant. This corresponds to conditions of high-viscosity-ratio and low density ratio. In Fig. 15, we compare this to our numerical results for $\rho_L/\rho_G = 5$, $\mu_L/\mu_G = 15$. To improve the comparison, we have modified the correlation by multiplying it by the internal circulation factor given in Eq. (4). This correlation significantly over-predicts the sensitivity to the Weber number for small Reynolds numbers. In the range $20 < Re < 200$, the results become more accurate. The derivation of this correlation was based on results at $Re = 10$, 20, 50, and 100 so accuracy in this range is expected. Because this correlation was derived assuming no liquid motion, it cannot be used to predict the drag for cases in which the liquid motion is important.

Haywood et al. neglected the liquid velocity in order to approximate contaminated drops. If this is a good approximation, our drag model can be used to predict contaminated drops by neglecting the effect of internal circulation on drag and deformation. Whether this approximation is accurate remains to be seen, but it does give an estimate of the possible effect of contaminants on drag. For cases that are sensitive to the liquid properties, such as $\rho_L/\rho_G = 500$, $\mu_L/\mu_G = 5$, contaminants could qualitatively and quantitatively change the results. For example, if we eliminate the liquid velocity, the drops would change from prolate to oblate and the drag correction would change from positive to negative. This has actually been observed in some of our

preliminary calculations with a contaminant model (Helenbrook and Edwards, 2000). Further work is necessary to examine these effects in detail.

8. Conclusions

We have performed over 3000 simulations to categorize the deformation and drag behavior of liquid drops. These simulations have been validated and give a precise picture of the drop deformation and drag response. Examining the deformation response, we found that there are three competing effects which determine the deformation of the drop. The first is a convective effect in the gas phase which causes oblate drops. The second is a convective effect in the liquid phase which causes prolate drops. The third is a combined effect of gas-phase viscous and convective forces. This is only important in large Ohnesorge number cases and tends to cause dimpled shapes to form.

We have developed an algebraic correlation which incorporates the first two effects and predicts the aspect ratio of the drop to within 10% (given the fluid properties, the drop volume, and the drop velocity). From this correlation we were able to more clearly understand the deformation properties of drops. For oblate cases, the primary parameter in predicting the aspect ratio is the Weber number. For the prolate cases, the aspect ratio is dependent on all of the parameters in the problem. Prolate cases are more likely to occur when the Ohnesorge number is small and $\rho_L/\rho_G(\mu_G/\mu_L)^2$ is large.

From this correlation we derived a simple criterion for the transition between prolate and oblate drops. This is an important transition because simple experiments with prolate ellipsoids have shown that they tumble as they fall through a gas while oblate ellipsoids are stable. Thus, we expect that when the drop transitions from prolate to oblate, a three-dimensional instability will occur. Using this criterion, we can predict the onset of this instability.

The aspect ratio of the drop is an important parameter in that it is necessary for predicting deformation corrections for mass, momentum, and heat transfer rates. We have used the aspect ratio correlation to incorporate the effects of deformation in estimating the drag of a drop. By combining the correlation with established results for the drag on an ellipsoid we were able to estimate the drag on a deformed liquid drop within 5% for moderate deformation cases and usually within 30% for high deformation cases in which the drag more than doubled relative to that of a solid sphere at the same conditions.

As part of the drag modeling effort, we also examined the effect of internal circulation on the drag of a spherical liquid drop. Several authors have examined this problem previously (Rivkind and Ryskin, 1976; Oliver and Chung, 1987) but previous correlations were not adequate for obtaining accurate results. For this reason, we created a new correlation for the effect of internal circulation on the drag. This correlation should prove useful for problems in which the liquid-to-gas viscosity ratio is greater than 5 and the Reynolds number is less than 200.

Acknowledgements

This work was supported in part by the Department of Energy under the ASCI/ASAP contract to Stanford University. Opinions expressed here are those of the authors and not of Stanford University or the Department of Energy.

References

Clift, R., Grace, J.R., Weber, M.E., 1978. Bubbles, Drops, and Particles. Academic Press.

Dandy, D.S., Leal, L.G., 1989. Buoyancy-driven motion of a deformable drop through a quiescent liquid at intermediate Reynolds numbers. J. Fluid Mech. 208, 161–192.

Grace, J.R., Wairegi, T., 1992. Shapes of fluid particles. In: Chhabra, R., Kee, D.D. (Eds.), Transport Processes in Bubbles Drops and Particles. Hemisphere Pub. Corp., pp. 133–145.

Haywood, R.J., Renksizbulut, M., Raithby, G.D., 1994. Numerical solution of deforming evaporating droplets at intermediate Reynolds numbers. Numer. Heat Transfer, Part A 26, 253–272.

Helenbrook, B.T., Mesh deformation using the biharmonic operator. Int. J. Num. Meth. Eng., in press.

Helenbrook, B.T., 2001. A two-fluid spectral element method. Comp. Meth. Appl. Mech. Eng. 191, 273–294.

Helenbrook, B.T., Edwards, C.F., 2000. A two-fluid spectral element method with application to drops. In: Proceedings of the 8th International Conference on Liquid Atomization and Spray Systems.

Hill, M.J.M., 1894. On a spherical vortex. Phil. Trans. Roy. Soc. (Lond.) A 185, 213.

Hsiang, L.P., Faeth, G.M., 1992. Near limit drop deformation and secondary breakup. Int. J. Multiphase Flow 18 (5), 635–652.

Johnson, T.A., Patel, V.C., 1999. Flow past a sphere up to a Reynolds number of 300. J. Fluid Mech. 378, 19–70.

Lamb, H., 1945. Hydrodynamics. Dover Publications, New York.

Miller, C.A., Scriven, L.E., 1968. The oscillations of a fluid droplet immersed in another fluid. J. Fluid Mech. 32, 417–435.

Oliver, D.L.R., Chung, J.N., 1987. Flow about a fluid sphere at low to moderate Reynolds numbers. J. Fluid Mech. 177, 1–18.

Rivkind, V.Y., Ryskin, G.M., 1976. Flow structure in motion of a spherical drop in a fluid medium at intermediate Reynolds numbers. Fluid Dyn. 11, 5–12.

Stone, H.A., 1994. Dynamics of drop deformation and breakup in viscous fluids. Ann. Rev. Fluid Mech. 26, 65–102.

Subramanyam, S.V., 1969. A note on the damping and oscillations of a fluid drop moving in another fluid. J. Fluid Mech. 37, 715–725.

Taylor, T.D., Acrivos, A., 1964. On the deformation and drag of a falling viscous drop at low Reynolds number. J. Fluid Mech. 18, 466–476.